Acta Materialia 265 (2024) 119643

Contents lists available at ScienceDirect

Acta Materialia

journal homepage: www.elsevier.com/locate/actamat

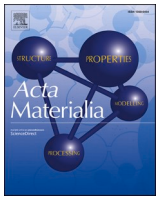

Full length article

The effect of shearable clusters and precipitates on dynamic recovery of Al alloys

Yixin Wang [a], Huan Zhao [b], Xinren Chen [b], Baptiste Gault [b,c], Yves Brechet [a], Christopher Hutchinson [a,*]

[a] Department of Materials Science and Engineering, Monash University, Victoria, 3800, Australia
[b] Max-Planck-Institut für Eisenforschung, Max-Planck-Str. 1, 40237 Düsseldorf, Germany
[c] Department of Materials, Imperial College, South Kensington, London SW7 2AZ, UK

ARTICLE INFO

Keywords:
Al alloys
Precipitation
Clusters
Dynamic recovery
SAXS
APT

ABSTRACT

The formability of Al alloys is strongly influenced by their strain hardening capacity. Whilst the effect of precipitates on yield strength has been thoroughly studied, their effects on the strain hardening behaviour have been comparatively less studied. This is especially true for the case of shearable particles, such as those formed during natural ageing, or underaging. This work presents a detailed study of the effect of shearable clusters/precipitates on the room temperature dynamic recovery of 7xxx Al alloys. The dynamic recovery behaviour is characterised by the slope of the stage III hardening (β) curve in a Kocks–Mecking plot, and the cluster/precipitate state has been characterised using small angle x-ray scattering and atom probe tomography. The rate of dynamic recovery is shown to depend non-monotonically on the yield strength of the alloy. For alloys in the solution treated and quenched state, or with an extremely fine distribution of clusters, dynamic recovery becomes more difficult with increasing alloy yield strength. However, as the cluster/particle spacing increases, such as during artificial ageing, dynamic recovery becomes easier. A phenomenological model is presented showing that the critical microstructural features controlling this non-monotonic dependence of dynamic recovery on yield strength is the ratio of the cluster/precipitate spacing and the critical annihilation distance between dynamically recovering dislocations. The model is general and describes well the experimental data. It can be used as a predictive tool to guide microstructure design for combinations of yield strength and strain hardening behaviour.

1. Introduction

Precipitate strengthened Al alloys find extensive use in transportation applications (planes, trains, and automobiles) as a means of light-weighting [1–3]. When designing components for these applications, the alloy strength (yield strength) is a critical factor, since it will determine the section thickness (and hence mass) required to carry a given load; the alloy durability, in terms of resistance to corrosion [4–7], fracture [8–14] and fatigue [11,15–17], is also important since it affects the component lifetime; and since many components need to be shaped by deformation processes (e.g. rolling, extrusion, forging), the formability is also a critical factor [18–22], especially when one is considering high strength alloys.

One may consider forming the alloy into its component shape in the soft state and then precipitation hardening after forming (e.g. the paint-bake cycle in automotive applications, e.g. [2,19,23–25]), or forming the alloy directly in its harder precipitate strengthened state. An intermediate case of warm forming, accompanied by dynamic precipitation is also possible [26–32]. Regardless of the strategy taken, the question of formability leads to two issues: the role of inclusions and their detrimental effect on fracture [8,12,19], and the role of strain localisation [33–40]. A key aspect of strain localisation is the ability of the alloy to strain harden during deformation, and strain hardening depends strongly on the precipitate state.

There is an abundant literature on the role of precipitation on the yield strength of alloys [41,42]. In the context of Al alloys, the effects of precipitate size and volume fraction [43–52], shape [49,53–57], and remaining solute in solution [58–63] have all been examined in great detail over the past 50 years. Whilst questions still remain, it should be generally seen as a major success of physical metallurgy to be able to design alloys and heat treatments to exploit solid state precipitation for a target yield strength.

* Corresponding author.
E-mail address: crh@monash.edu (C. Hutchinson).

https://doi.org/10.1016/j.actamat.2023.119643
Received 30 October 2023; Received in revised form 27 December 2023; Accepted 28 December 2023
Available online 29 December 2023

By comparison, the effect of precipitation on strain hardening in Al alloys has been much less studied [64,65]. This is all the more complicated because of the dual nature of strain hardening – there is a kinematic contribution stemming from internal stresses (largely generated by shear-resistant particles [33,34,66–76]), and an isotropic component arising from the dynamics of dislocation accumulation and storage [34,66–68,75–78]. The internal variable models (such as the Kocks–Mecking-Estrin (KME) model [77,79,80]) have proven a versatile and successful tool for describing the isotropic contribution to the strain hardening.

The effects of precipitates on the strain hardening depends on the nature of the precipitates. When the precipitates are shear-resistant, they strongly increase dislocation storage [33,34,66–69,74–76,78]. A kinematic contribution to the strain hardening develops (and then saturates with strain) due to the elastic loading of the precipitates [33,67,68,71–75], and the precipitates covered in dislocation loops are thought to accelerate dynamic recovery [78]. A reasonable understanding of these effects now exists.

When the precipitates are shearable, the effect on strain hardening is much less clear, especially when it comes to considerations of their effects on dynamic recovery. Dynamic recovery requires the interaction stress between two dislocations to exceed the resistance stress between them to come together and annhiliate. One proposal is that the resistance stress is proportional to the yield strength. This means that as one precipitate hardens an alloy by forming a distribution of shearable particles, dynamic recovery becomes more difficult [78,81]. An alternative proposition considers a possible indirect effect of the precipitates. As precipitation hardening occurs, solute is removed from solid solution. This solute removal may increase the stacking-fault energy and make cross-slip easier, facilitating dynamic recovery [77]. This proposal would make dynamic recovery easier as the yield strength increases during precipitation. As will be shown in this contribution – dynamic recovery actually shows a non-monotonic dependence on yield strength.

Here we study in detail the dynamic recovery behaviour of a number of Al alloys at room temperature, with various states of precipitation, and provide a simple microstructure-based model to describe the effects of shearable clusters/particles on dynamic recovery. Naturally aged alloys (containing shearable clusters), as well as alloys underaged at elevated temperature (containing shearable precipitates) are both considered. Even when an Al alloy is formed in its soft state, after solution treatment and quenching but before artificial ageing, some natural ageing inevitably occurs. This natural ageing introduces clusters into the microstructure and they affect the strain hardening. When an alloy is instead formed into shape in its hardened state, it already contains a high number density of fine particles. In the 2xxx, 6xxx and 7xxx alloys, the states leading up to the peak aged states are usually dominated by shearable particles [3], and a detailed understanding of their effect on strain hardening, and in particular dynamic recovery, is required to understand formability. There is a second reason for the interest in the strain hardening of alloys already strengthened by precipitates – this also affects the energy absorbed during deformation and hence the crashworthiness of vehicles [2,82]. This is especially important for the automotive industry.

2. Experimental procedure

2.1. Materials and treatments

The Al alloys considered in this study and the compositions of the main elements are listed in Table 1. All alloys are commercial grades either purchased or donated. The most detailed analysis is performed on AA7050 (a high strength Al-Zn-Mg-(Cu) alloy) and this was received in the form of a hot-rolled plate. The AA7050 samples were solution treated for 1 h at 480 °C followed by water quenching (STQ). Some samples underwent natural ageing (NA) at 25 °C or artificial ageing at 150 °C for different times to create microstructures containing shearable clusters or precipitates (Table 2). The condition of 150 °C ageing for 10 h corresponds to the peak aged state (PA) for this alloy.

Table 1
Chemical compositions of the main elements in the Al alloys considered in this study. The compositions of Al alloys labelled * were measured by ICP-AES. The other alloy compositions were supplied by the manufacturer.

Alloy	Composition (wt.%)				
	Cu	Mg	Zn	Mn	Si
AA7050*	2.2	2.3	6.2	0.05	0.06
AA5083	0.1_{max}	4.0–4.9	0.25_{max}	0.4–1.0	0.4–0.7
AA6061*	0.24	1.0	0.04	0.05	0.67
AA7075	1.2–2.0	2.1–2.9	5.1–6.1	0.3_{max}	0.4_{max}
AA7040	1.5–2.3	1.7–2.4	5.7–6.7	0.04_{max}	0.1_{max}
AA7020	0.2_{max}	1.0–1.4	4.0–5.0	0.05–0.5	0.35_{max}

Additional commercial 7xxx Al alloys AA7075, AA7040 and AA7020 were also investigated in their NA and artificially aged states to test the generality of the model to be presented. AA5083, AA6061 and AA7075 were examined in their STQ states. Samples of AA5083 and AA6061 were solution treated for 1 h at 350 °C and 530 °C, respectively, and samples of AA7075, AA7040 and AA7020 were solution treated for 1 h at 480 °C, followed by water quenching. The specific ageing conditions for the four 7xxx alloys are listed in Table 2. All samples were stored in a freezer at −35 °C after heat treatment and prior to testing to minimise any additional natural ageing.

2.2. Mechanical testing

Monotonic tensile tests were conducted on a servo-hydraulic MTS Landmark machine with a 100 kN load capacity and an alignment fixture. It is particularly important for studies of strain hardening that an especially well aligned testing system is used. The alignment of the MTS was calibrated to be close to ASTM E1012 Class 5 (i.e. maximum bending strain smaller than 5% of the total strain) and the alignment was repeated periodically during the testing schedule. All tests were performed at room temperature (25 °C) with a crosshead speed of 0.02 mm/s (equivalent strain rate $\sim 1.3 \times 10^{-3}$ s^{-1}). Cylindrical tensile samples with a gauge length of 15 mm and a gauge diameter of 5 mm were machined with the loading direction parallel to the rolling or extrusion direction. 2 to 4 samples were tested for each condition and alloy to test reproducibility and this is reflected in the error bars for the data to be reported.

Bauschinger tests were performed to quantify any kinematic contributions to the strain hardening. The tests were conducted using the same MTS Landmark machine with the same crosshead speed as the tensile tests. Cylindrical samples with a gauge length of 18 mm and a gauge diameter of 9 mm were machined with the loading direction parallel to the rolling or extrusion direction. Two clip-on extensometers were mounted diametrically opposed to each other so that buckling during compression can be identified once the signals from the two extensometers deviate from each other significantly [75,83]. For all the data to be reported, any internal stress measured from the Bauschinger tests

Table 2
Natural ageing (NA) and artificial ageing conditions of the AA7050, AA7075, AA7040 and AA7020 alloys.

Alloy	Ageing condition	
AA7050	NA	6 h, 12 h, 24 h, 48 h, 106 h, 792 h, 1670h
	150 °C	10 min, 0.5 h, 2 h, 5 h, 10 h (PA)
AA7075	NA	12 h, 24 h, 48 h, 122 h, 360 h, 720 h, 1yr
	120 °C	10 min, 0.5 h, 2 h, 5 h, 24 h (PA)
	150 °C	0.5 h, 2h
AA7040	NA	6 h, 12 h, 24 h, 48 h, 120 h, 1yr
	150 °C	10 min, 0.5 h, 1 h, 2 h, 5h
AA7020	NA	7 h, 12 h, 24 h, 47h
	150 °C	0.5 h, 1 h, 2h

represents less than 10% of the strain hardening increment. This provides confidence that the dynamic recovery being studied is occurring in a system where the strain hardening is dominated by isotropic hardening effects.

2.3. Microstructural characterisation

2.3.1. Small-angle X-ray scattering (SAXS)

SAXS is a tool that allows us to characterise nm-sized particles from volumes of material relevant for studies of plasticity and therefore provides some confidence in the statistical relevance of the precipitate measures.

SAXS experiments were conducted on all the AA7050 states except the STQ, NA24h, NA792h and 150 °C 2 h states. SAXS samples were cut from the head part of tensile samples and ground to ~70 μm thickness. This thickness provides a ~30% Cu x-ray transmission rate. The SAXS experiments used a Bruker N8 Horizons SAXS system with a Cu-anode X-ray source. The SAXS patterns were recorded on a two-dimensional detector (Vantec-500). The signals were radially averaged and plotted as a function of the scattering vector, q. The data were corrected for background noise, transmission rate and specimen thickness. A constant Laue scattering intensity from the solid solution was subtracted to isolate the clusters/precipitates contribution to the scattered signal. The AA7050 PA (10 h 150 °C) sample was used as an internal standard for absolute intensity calibration by assuming that its precipitate composition and volume fraction is close to the local equilibrium state for the η' phase at 150 °C, which was calculated using the Thermo-Calc 2021a TCAL4 database: $f_v = 6.4\%$, $C_{ppt}^{Mg} = 28$ *at.*%, $C_{ppt}^{Zn} = 39$ *at.*%, $C_{ppt}^{Al} = 33$ *at.*%. The reasonableness of this is justified in a following section.

The SAXS data was represented in the form of a Kratky plot, i.e. Iq^2 vs. q where q is the scattering vector ($Å^{-1}$) and I ($Å^{-3}$) is the scattered intensity. SAXS was used to estimate the size and volume fraction of clusters/precipitates [84,85]. With the assumption that the clusters/precipitates detected can be approximated as spheres and present with a reasonably narrow size distribution, their size can be estimated by the Guinier radius R_g obtained from the scattering vector q_m at which Iq^2 shows a maximum [84]:

$$R_g = \frac{\sqrt{3}}{q_m} \tag{1}$$

Considering a two phase material composed of particles with electron scattering density ρ_p embedded in a matrix of electron scattering density ρ_m, the volume fraction of objects is estimated using the integrated scattered intensity Q [84]:

$$Q = \int_0^\infty Iq^2 dq, \quad Q = 2\pi^2 |\rho_p - \rho_m|^2 f_v (1 - f_v) \tag{2}$$

Determining the cluster/precipitate volume fraction requires knowledge of the electron scattering density of the matrix and precipitates, and this requires knowledge of their compositions. This is especially difficult for nanometre sized particles.

Two estimates for the cluster or precipitate composition are made:

a) we assume that the cluster/precipitate compositions in all tested states of the AA7050 alloy are close to the η' phase at 150 °C calculated using Thermo-Calc, and Q can then be calculated using Eq. (3). A similar composition has previously been assumed for the GP zones in an AA7010 alloy [86].

$$Q = \frac{Q^{PA}}{f_v^{PA}\left(1 - f_v^{PA}\right)} \cdot f_v (1 - f_v) \tag{3}$$

b) Atom probe tomography is used to experimentally measure the cluster/precipitate compositions for two states of the AA7050 alloy. This should also be considered an estimate of the composition, and the approach taken is described in detail below.

2.3.2. Atom probe tomography (APT)

The NA 1670 h and 150 °C 10 min states of AA7050 alloy were selected to conduct APT experiments to assess for changes in the clusters/precipitates chemistry for the different treatments (naturally aged versus artificially aged). APT specimens were prepared on a FEI Helios Plasma focused ion beam (PFIB) using a Xe source. APT experiments were conducted on a Cameca Instrument Inc. Local Electrode Atom Probe (LEAP) 5000XS at a base temperature of 40 K in voltage-pulsed mode. The pulse fraction, pulse rate and target detection rate of the measurement were 20%, 250 kHz and 0.5%, respectively.

Data reconstruction and analysis of the 1st nearest neighbour distribution and radial distribution function (RDF) were performed using the AP suite software. The 'distribution of isolated atoms for the determination of the matrix composition' (DIAM) method [87] combined with the pair correlation function (PCF) protocol [88,89] was used to estimate the matrix and cluster/precipitate chemistries. We follow the approach in [88], where the pair correlation function, γ, of species $i-j$ pair, $\gamma_{i-j}(r)$, is defined as:

$$\gamma_{i-j}(r) = \overline{C_i} \cdot C_{i-j}(r) - \overline{C_i} \cdot \overline{C_j} \tag{4}$$

where $\overline{C_i}$, $\overline{C_j}$ are the average compositions of element i and j, and $C_{i-j}(r)$ is the concentration of species j at a distance r from an atom of species i averaged over all the atoms of species i. In the case of the correlation between the same species:

$$\gamma_{i-i}(r) = \overline{C_i} \cdot C_i(r) - \overline{C_i}^2 \tag{5}$$

Eq. (5) can be written in terms of two contributions [88]:

$$\gamma_{i-i}(r) = \overline{\Delta C_i^2} \cdot \gamma_0(r) \tag{6}$$

$\gamma_0(r)$ is the shape function of the PCF which is dependent only on the geometry of the objects. For spherical particles of radius R, $\gamma_0(r)$ is represented by $\gamma_0^{sphere}(r,\ R)$ and is given as [90]:

$$\gamma_0^{sphere}(r) = \begin{cases} 1 - \dfrac{3r}{4R} + \dfrac{r^3}{16R^3} & (r \le 2R) \\ 0 & (r > 2R) \end{cases} \tag{7}$$

$\overline{\Delta C_i^2}$ is the mean square composition fluctuation dependent only on the quantity and composition of the objects:

$$\overline{\Delta C_i^2} = f_v (1 - f_v)\left(C_p^i - C_m^i\right)^2 = \left(C_p^i - \overline{C_i}\right)\left(\overline{C_i} - C_m^i\right) \tag{8}$$

In Eq. (8), C_p and C_m refer to the particle and matrix compositions, respectively, and f_v is the volume fraction of particles. In this contribution, C_m^i was determined by the DIAM method [87], with an associated error bar, and this uncertainty is propagated through the calculations of C_p and f_v and is reflected in the error bars on those quantities.

It has been shown that for particles of radius of 1 nm and smaller, the limited spatial resolution of APT can significantly change the PCF shape (Eq. (7)) and distort the particle size and composition [89,91]. As a result, we model the limited spatial resolution by convoluting the PCF shape with a resolution function [89]. We assume that there is a single type of particle of radius equal to R_g obtained from the SAXS data, which enables a determination of the analytical PCF shape. We further assume that the spatial resolution function has a Gaussian distribution with a standard deviation σ. By convoluting the analytical PCF shape with the resolution function in three-dimensional coordinates, one obtains a resolution-affected PCF shape $\gamma_0^{ResConv}(r)$. As a result, $\overline{\Delta C_i^2}$ can be

calculated by fitting $\gamma_{i-i}(r)$ with $\gamma_0^{ResConv}(r)$:

$$\gamma_{i-i}(r) = \overline{\Delta C_i^2} \cdot \gamma_0^{ResConv}(r) \quad (9)$$

The set of $\overline{\Delta C_i^2}$ gives the C_p^i and a set of volume fractions calculated for each solute element. Since we assume that there is only a single type of particle, we fix the volume fraction as an average of those computed from Eq. (8) with Mg and Zn. Cu is excluded from the averageing due to its low content, both on average and in the precipitates. With this "consolidated" volume fraction, the corrected C_p^i are recalculated from Eq. (8).

3. Results

3.1. Mechanical response

The room temperature tensile response of all alloys tested, expressed as true-stress versus true-strain is shown in Fig. 1a–c. AA7050 shows an increase in yield strength, ultimate tensile strength (UTS) and uniform elongation as a function of NA time (Fig. 1a). Similar observations are made by Zhang et al. [92]. AA7050 artificially aged at 150 °C, also shows an increase in yield strength and UTS as a function of ageing time, but in this case the uniform elongation decreases as the yield strength increases. The tensile response of AA7050, AA7075, AA5083 and AA6061, all in the STQ state, is shown in Fig. 1c. These alloys contain different solute types and levels (Table 1) and provides an indication of the effect of solute in solution on the dynamic recovery behaviour.

The corresponding strain hardening behaviour, expressed in the form of so-called Kocks–Mecking (KM) plots [77,79,80], is shown in Fig. 1d–f. In all cases, except AA7050 PA (10 h at 150 °C), the stage III strain hardening behaviour is well represented as a straight line in the KM plot. In the case of the STQ alloys (Fig. 1f), dynamic strain ageing effects are evident due to the larger concentrations of solute in solution and this is the reason for the fluctuations in the KM curves.

Bauchinger tests have also been performed on a selection of these alloys to test for any significant kinematic contribution to the strain hardening. These Bauschinger plots are shown in the Supplementary materials. The only state shown in Fig. 1 where a significant kinematic hardening contribution is observed is the PA (10 h 150 °C) AA7050 state. This kinematic contribution is also the reason for the non-linear Stage III curve in the KM plot of the AA7050 PA state in Fig. 1e. Due to this kinematic contribution, the PA state is excluded from the analysis reported in subsequent sections. This PA state of AA7050 represents the state where a non-negligible fraction of the precipitates begin to be bypassed and this leads to a qualitative change in the strain hardening behaviour.

The dynamic recovery behaviour of a material showing isotropic strain hardening can be characterised by the slope of the Stage III curve (β) in a KM plot [33,67,77,78]. An example is indicated in Fig. 1e for the 10 min 150 °C AA7050 (β=5.05) state. β has been quantified for all states and is plotted as 1/β versus the experimentally measured yield strength in Fig. 2. The error bars represent the range of β measured on the 2–4 samples tested for each state. Where an error bar cannot be seen, the error is smaller than the data point size in the plot.

Fig. 2 brings together four groups of data: the AA7050 in the NA state (Fig. 1a, d), the AA7050 after ageing at 150 °C (Fig. 1b, d), four STQ alloys (AA7050, AA7075, AA6061 and AA5083) (Fig. 1c and f), as well as some data on STQ alloys taken from the literature (AA1100, AA5005, AA5052 and AA5754). All of the data falls on a master curve showing a proportionality between 1/β and the experimentally measured yield strength up to ~300 MPa (indicated by the grey dashed line). In particular, all of the single phase or STQ alloys lie on the same master

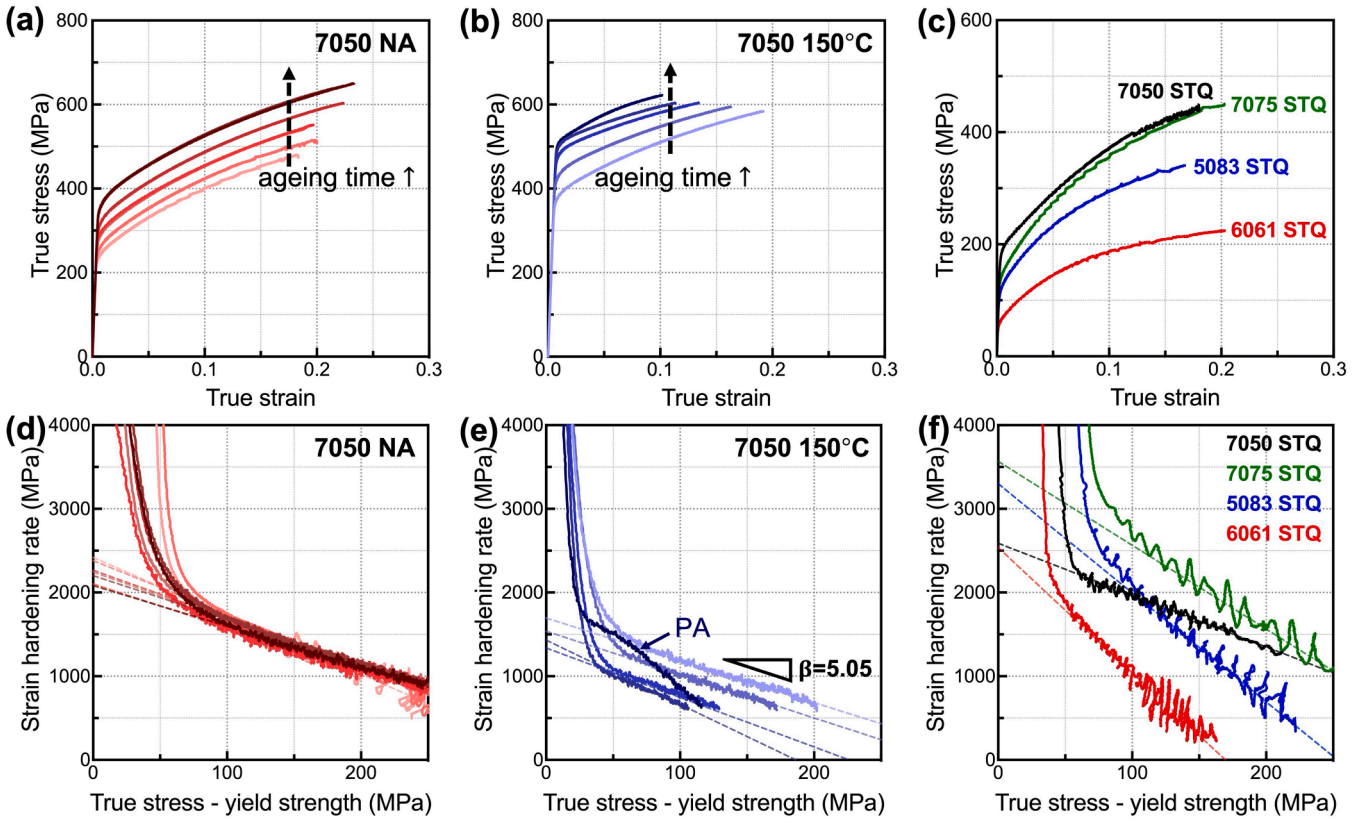

Fig. 1. True stress strain curves of (a) AA7050 alloy NA for 6 h, 12 h, 24 h, 48 h, 106 h, 792 h and 1670 h; (b) AA7050 alloy 150 °C aged for 10 min, 0.5 h, 2 h, 5 h and 10 h; and (c) STQ states of AA7050, AA7075, AA5083 and AA6061. (d-f) The corresponding Kocks–Mecking (KM) plots. The dashed lines in (d-f) show the linear trend of the stage III work hardening, of which the slope (β) was used to characterise materials dynamic recovery behaviour in this work. An example of β quantification for the AA7050 150 °C 10 min state is indicated in (e).

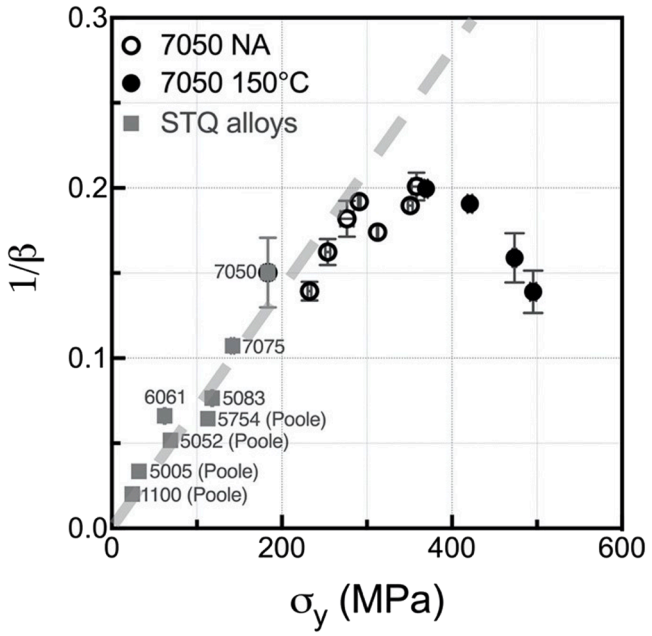

Fig. 2. Evolution of the experimental $\frac{1}{\beta}$ as a function of σ_y for the AA7050 NA states (open circles), AA7050 150 °C aged states (full circles), and other Al alloys in the STQ states (grey squares). Error bars originate from multiple tensile tests. Data points of AA1100, AA5005, AA5052, AA5754 were taken from Poole [65].

curve, even though they come from different Al alloy classes (1xxx, 5xxx, 6xxx and 7xxx) and contain very different solute contents and types of solute in solid solution. This strongly suggests that the first order effect on dynamic recovery is the yield strength and not any solute effect on the stacking fault energy. At yield stresses higher than 300 MPa, the dependence reverses and 1/β decreases with further increases in yield strength. As the yield strength of the Al alloys shown in Fig. 2 increases up to ~300 MPa, regardless of whether the source of the strengthening is solid solution strengthening (STQ alloys) or cluster strengthening in the NA AA7050 states, dynamic recovery becomes more difficult (1/β increases). This retardation of dynamic recovery with the increase in yield strength due to NA of the AA7050 alloy is the reason why the uniform elongation, as well as the yield strength and UTS, all increase simultaneously in Fig. 1a.

After artificial ageing of the AA7050 at 150 °C, dynamic recovery becomes easier (1/β decreases) as the yield strength increases. This is the reason why the uniform elongation decreases with increasing yield and tensile strength in Fig. 1b.

The proportionality between 1/β and the yield strength (up to ~ 300 MPa) in Fig. 2 is consistent with previous suggestions [78,81] that the resistance stress seen by dislocations undergoing a dynamic recovery event is proportional to the yield strength. As a result, as the yield strength increases, dynamic recovery becomes more difficult. To understand the non-monotonic behaviour in Fig. 2 requires a detailed characterisation of the precipitate and cluster state and consideration of their effect on the dynamic recovery process.

3.2. SAXS characterisation of particle size and inter-particle spacing

SAXS was used to characterise the cluster/precipitate state for most of the NA and artificially aged AA7050 states. Since we are interested in questions of plasticity, and plasticity occurs on a length scale of microns and tens of microns, it is important to also characterise the average precipitate state over this length scale. SAXS is a very good tool for this reason. The Kratky plot in Fig. 3 allows us to estimate the mean scattering object size from the peak position (Eq. (1)), and the volume

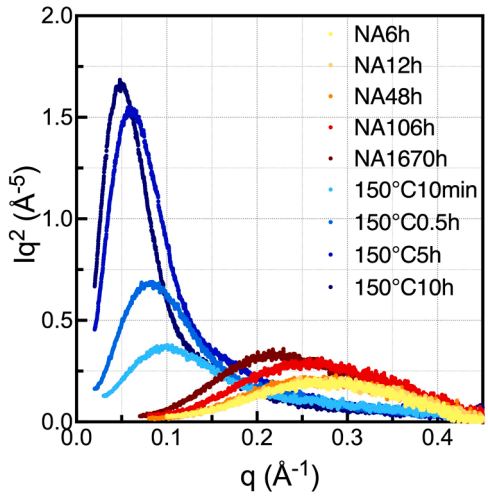

Fig. 3. SAXS data expressed in the form of a Kratky plot ($\mathbf{Iq^2}$ **vs.** $\mathbf{q}$) for the AA7050 NA and 150 °C aged states.

fraction of scattering objects is related to the total scattered intensity, which depends on the area under the curves (Eq. (3)).

The average particle size, expressed as the Guinier radius, and volume fraction for each of the AA7050 states shown in Fig. 3 have been quantified using Eqs. (1) and (3) and are plotted in Fig. 4a and b, respectively. To quantify the volume fraction of objects, one must know the composition of the particles and matrix. The first estimate we make is to assume that the clusters (in the NA state) and the precipitates in the artificially aged states (150 °C) all have exactly the same composition and this composition corresponds to the composition of η' phase at 150 °C, calculated using the Thermo-Calc 2021a TCAL4 database: $C_{ppt}^{Mg} = 28\ at.\%, C_{ppt}^{Zn} = 39\ at.\%, C_{ppt}^{Al} = 33\ at.\%$. Using this estimation for the composition of the particles, the volume fractions are shown in Fig. 4b. The volume fraction of particles at the longest NA time (1670 h) is approximately the same as the volume fraction of particles after 10 min of ageing at 150 °C. Of course, the sizes of the particles during NA are much smaller than those observed during artificial ageing. The error bands indicated in the volume fraction plots of Fig. 4b correspond to ± 20% of the integrated intensity from the SAXS measurements. This error bar is included to capture the uncertainty in quantifying the Laue scattering from the solid solution, e.g. [93], which is subtracted from the total scattered intensity to isolate the scattering coming from the clusters/precipitates.

Assuming the particles can be approximated as spherical, the number density of particles can be calculated from the size and volume fraction, along with the average spacing between particles. These are shown in Fig. 4c and d, respectively, and will be used in the subsequent modelling. The number density of clusters in the NA state is $\sim 10^{25}$ (m^{-3}) and the number density of precipitates after artificial ageing is $\sim 10^{24}$ (m^{-3}). These are consistent with previous measurements on 7xxx alloys (e.g. [27,86,94–96]). As expected from such number densities, the spacing between clusters/particles (Fig. 4d) is much smaller for the NA state than the artificially aged state of AA7050 (Fig. 4d).

The quantification of cluster/precipitate characteristics shown in Fig. 4 assumes that the chemistry of the clusters/precipitates in the NA and artificially ages states is the same.

3.3. APT characterisation

To obtain an experimental estimate of the cluster/precipitate chemistries, we used atom probe tomography for two states of the AA7050 alloy: NA 1670 h and 10 min 150 °C. Reconstructured APT maps for these two states are shown in Fig. 5. The NA state (Fig. 5a)

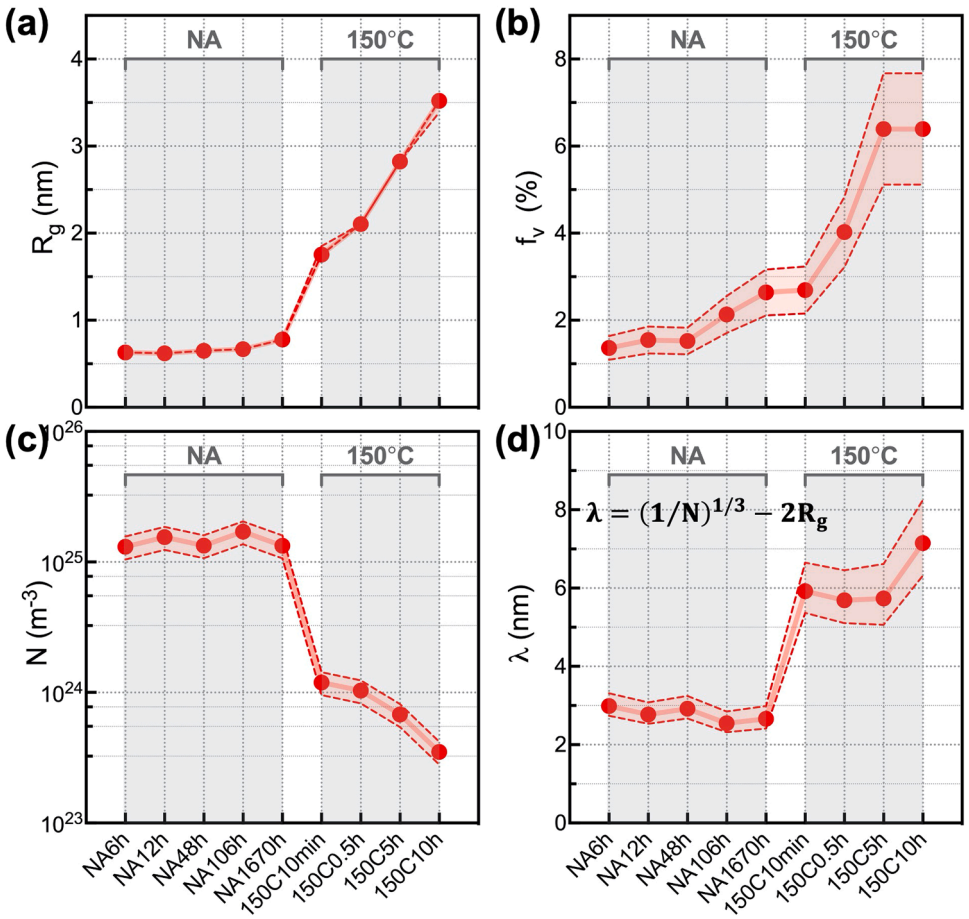

Fig. 4. (a) The Guinier radius $\mathbf{R_g}$, (b) volume fraction $\mathbf{f_v}$, (c) number density **N** and (d) inter-particle spacing λ of the clusters/precipitates for the AA7050 NA and 150 °C aged states obtained by SAXS, with the particle chemistry assumed to be the same as the equilibrium η' phase calculated by Thermo-Calc. The error band range represented in b-d arises from an assumption of an error bar of ±20% on the SAXS integrated intensity used to calculate the volume fractions.

contains numerous small objects, as expected from the SAXS (Fig. 4a and c), but their compositions cannot be readily estimated from the elemental maps. In the artificially aged state (Fig. 5b) the imaged particles have a radius of approximately 2 nm, which agrees well with the SAXS measurements (Fig. 4a). The particles in the artificially aged sample are enriched in Zn and Mg but no obvious Cu incorporation is observed from the Cu map shown in Fig. 5b.

As discussed by de Geuser and co-workers [89,91], estimating the chemistry of such small objects using APT is not straightforward. We follow the approach outlined in [89], and summarised in the experimental method section, but it must be emphasised that these measurements are best estimates using the most current analysis protocols.

Fig. 6 presents the pair correlation functions (PCF, γ) for the two AA7050 samples along with the corresponding fits (Eq. (9)). The three fitting curves for each element and state were obtained by convoluting a Gaussian spatial resolution function with a standard deviation, σ. Three different standard deviations are shown: σ=0.5, 0.6, 0.7. The overall best fit to the experimental data was generally achieved with σ=0.6. It is noted that the PCF fit for the Zn-Zn pair of the 150 °C 10 min state appears less good (in terms of shape but not intercept), which is likely due to the fact that precipitates have a size distribution (e.g. following a log-normal distribution) instead of being monotonically distributed. The precipitates are more enriched in Zn than Mg, which means the PCF fit for Zn (compared with Mg or Cu) is more influenced by the size distribution. However, since we have introduced a fitting parameter σ from the spatial resolution function, we choose not to consider the particle size distribution so as to avoid introducing more fitting paramters. Based on the amplitudes of the PCF (γ(0)), the clusters/precipitates in both samples mainly consist of Zn and Mg, with only small amounts of Cu. Note that the y-axis scale of Fig. 6a and b is different (x10^{-4} in Fig. 6a and x10^{-3} in b). The amplitudes of the PCF (γ(0)) indicate that the particles formed in the 150 °C 10 min sample are more enriched in Zn and Mg than the clusters formed in the 1670 h NA state of the AA7050.

Quantification of the global composition of each APT specimen, matrix composition and cluster/precipitate compositions using the DIAM-PCF protocol (outlined in the experimental method and [88,89]) are shown in Fig 7. Fig. 7a contains a dashed and solid line for each solute element. The dashed line represents the global composition of that solute element measured in the APT tip, and the solid line represents the composition of that solute element measured in solid solution in the same APT tip. As should be the case, the solid lines fall below the dashed lines for each element. The solid lines include an error band, and this represents the uncertainty in quantification of the solid solution concentration using the DIAM method. We can see from Fig. 7a that more solute has been removed from solid solution by precipitation in the case of the 150 °C 10 min sample, compared to the NA 1670 h sample. The cluster/precipitate compositions for both states are presented in Fig. 7b. The error bars shown in Fig. 7b result from propagating the errors in Fig. 7a regarding the matrix solid solution compositions through the PCF protocol. Precipitates in the 150 °C 10 min state comprise about 21 at.% Mg, 30 at.% Zn and 5 at.% Cu, which corresponds well to the equilibrium η' phase composition. Clusters in the NA1670h sample consist of about 14 at.% Mg, 21 at.% Zn and 6 at.% Cu, approximately 2/3 the composition of the equilibrium η' phase.

With these experimental estimates of the cluster/precipitate compositions measured using APT, the SAXS data can be reanalysed for these

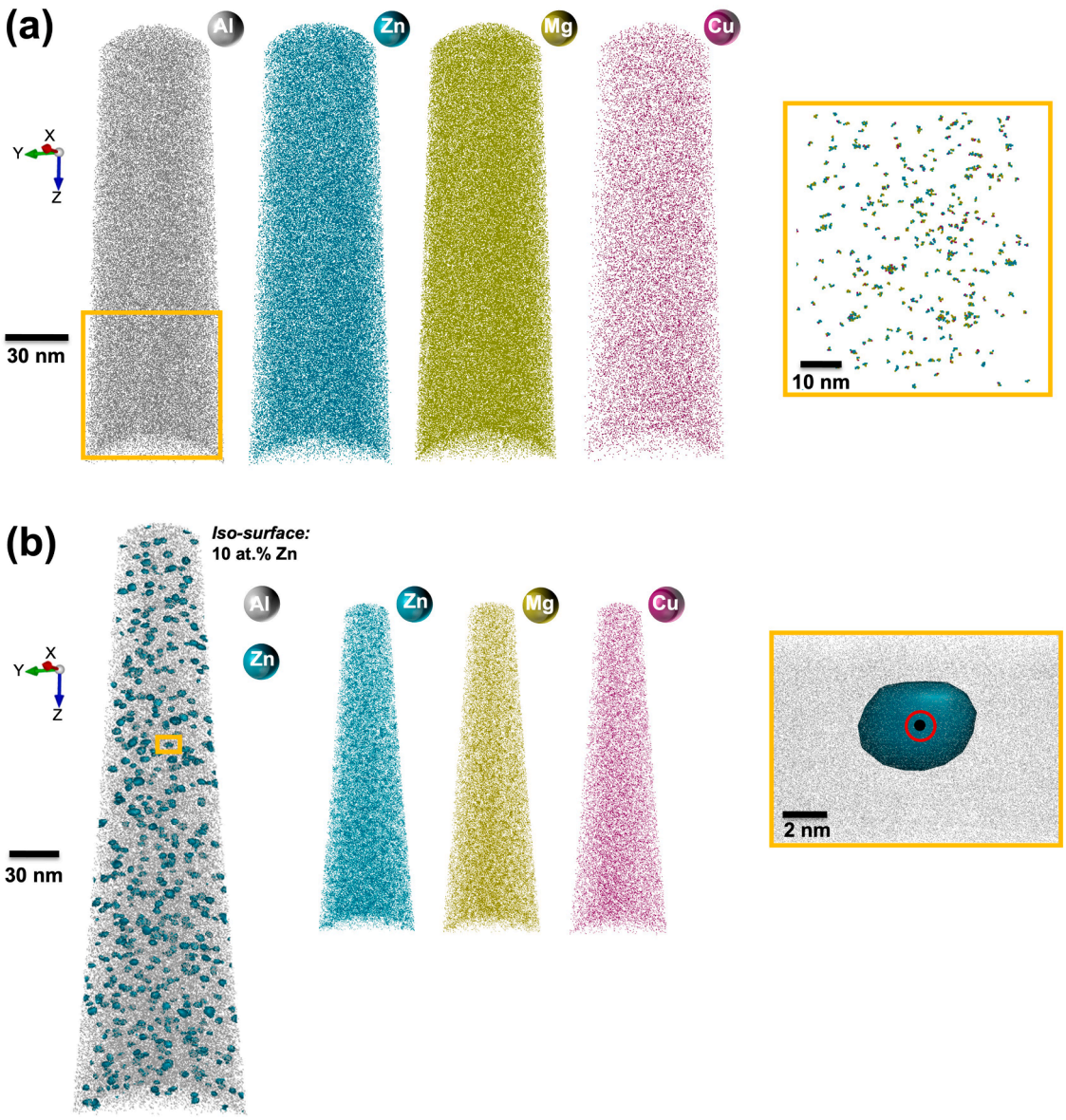

Fig. 5. APT maps for the (a) NA 1670 h and (b) 150 °C 10 min states of AA7050 showing the arrangement of solute atoms. Representative clusters and precipitate are shown in the yellow rectangles in a and b respectively.

two states and a second estimate of the cluster/precipitate volume fraction, number density and particle spacing can be obtained. Both estimates (those using the η' compositions from Thermo-Calc, and the estimates using the APT particle compositions measurements) are shown in Fig. 8. Since the 150 °C 10 min sample has an estimated particle chemistry from APT close to the Thermo-Calc η' phase, the results of these two approaches show excellent agreement. However, in the NA 1670 h sample, because APT estimates a significantly more dilute cluster chemistry compared to the η' phase, this leads to higher estimated volume fraction and number density (Fig. 8a and b), resulting in a further reduction in the spacing between clusters (Fig. 8c).

4. Discussion and modelling

The proportionality between 1/β and the macroscopic yield strength (up to ~300 MPa) shown in Fig. 2 is consistent with previous suggestions of Deschamps et al. [81] and Simar et al. [78] that the resistance stress seen by dislocations undergoing a dynamic recovery event may be proportional to the yield strength. This idea can describe the room temperature dynamic recovery behaviour of a wide range of STQ Al alloys, as well as the AA7050 in most of the NA states (Fig. 2). In the following, we build a simple model based on this idea, and introduce a key new ingredient to explain the deviation that leads to the non-monotonic 1/β as the yield strength further increases above 300 MPa in Fig. 2.

4.1. Modelling the effect of yield strength on dynamic recovery considering the inter-particle spacing effect on dislocation annihilation

As summarised by Simar et al. [78], in the KME framework, the dynamic recovery rate, β, is proportional to the critical distance (y*) that two dislocations of opposite sign must approach to be able to annihilate. If dislocations can annhiliate even when separated by a large distance (ie. large y*), then dynamic recovery is quite easy. If dislocations need to approach very close to each other (i.e. a small y*) for an annhiliation event to occur, then dynamic recovery is more difficult.

This critical distance, y*, is such that the interaction stress between the dislocations ($\propto Gb/y^*$), where G is the Shear modulus and b is the Burgers vector, exceeds the resistance stress felt by the dislocations (σ_y^*).

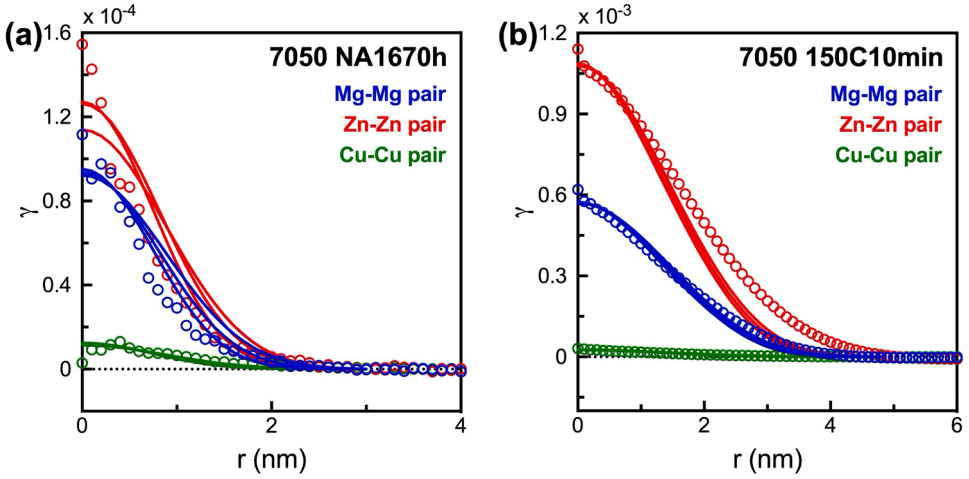

Fig. 6. Experimental (circles) and fit (lines) APT pair correlation functions (γ) for the Mg-Mg, Zn-Zn and Cu-Cu pairs of the (a) NA 1670 h and (b) 150 °C 10 min states of AA7050. The three fitting curves of each solute pair and state were obtained by convoluting a Gaussian resolution function with a standard deviation $\sigma = 0.5$, 0.6, 0.7, respectively. The best fit to the experimental data was achieved at $\sigma = 0.6$.

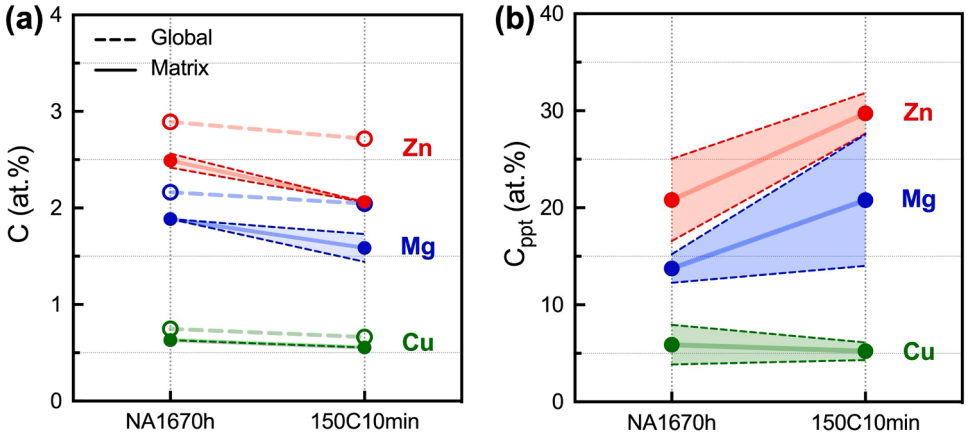

Fig. 7. (a) The global compositions (open circle with dashed line) and the range of matrix compositions (full circle with full line) of the AA7050 NA 1670 h and 150 °C 10 min states measured using APT. The error band on the solid lines represents the uncertainty in the solid solution concentration using the DIAM method. (b) The clusters/precipitates compositions of the AA7050 NA 1670 h and 150 °C 10 min states measured using APT. The error bars shown in Fig. 7b result from propagating the errors in Fig. 7a regarding the solid solution compositions through the PCF protocol.

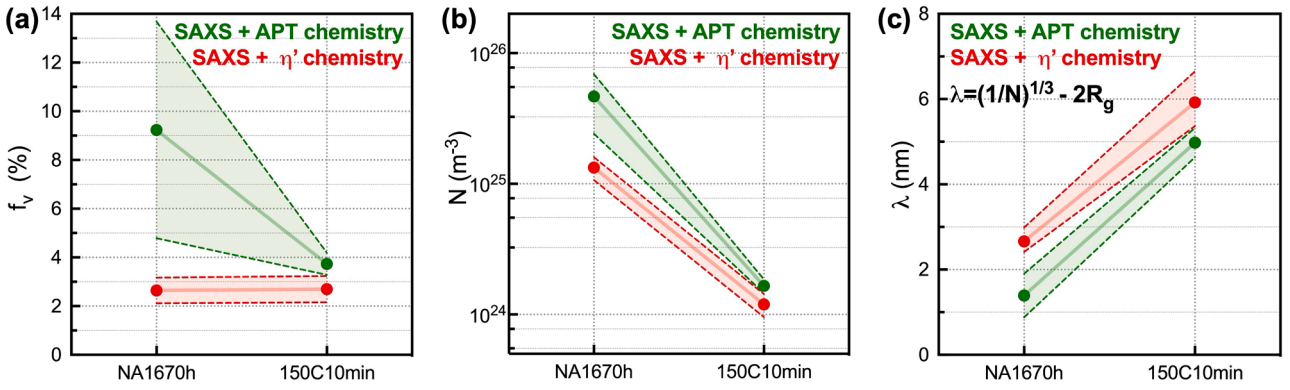

Fig. 8. (a) The volume fraction $\mathbf{f_v}$, (b) number density **N** and (c) inter-particle spacing λ of clusters/precipiates in the AA7050 NA1670h and 150 °C10min states obtained by SAXS with the particle chemistry obtained by APT (green), and with the particle chemistry assumed to be the equilibrium η' phase calculated by Thermo-Calc (red) (For interpretation of the references to colour in this figure legend, the reader is referred to the web version of this article.).

This leads to the dynamic recovery rate β to be inversely proportional to the local resistance stress σ_y^* as shown in Eq. (10). The proportionality factor k_β describes how much more difficult it is for the dislocations to be annihilated by dynamic recovery compared to their in-plane slip. If the resistance stress seen by the dislocations, σ_y^*, is equal to the experimentally measured yield strength, then Eq. (10) corresponds to the dashed grey line in Fig. 2 that describes well the dynamic recovery of all the states with yield strengths up to ~300 MPa, k_β=19.3.

$$\frac{1}{\beta} = k_\beta \frac{\sigma_y^*}{G} \tag{10}$$

For coarse grained, STQ alloys it seems reasonable that the resistance stress seen by the dislocations undergoing a dynamic recovery event, is proportional to the experimentally measured yield strength. The matrix is spatially quite uniform, even at the length scale of y*. However, once particles are introduced into a matrix, the situation changes. Consider the schematic shown in Fig. 9 which presents two extreme cases of two dislocations separated by a critical annhiliation distance (y*) in matrices containing particles with different interparticle spacings, λ. Fig. 9a shows a situation where the spacing of clusters/precipitates, λ, is significantly smaller than the critical dislocation annihilation distance y*. In such a situation, the particles serve as obstacles impeding dislocation annihilation and the resistance stress felt by the dislocations would be similar to the macroscopically measured yield strength. However, Fig. 9b shows a situation where the spacing of particles λ is much larger than y*. In this case, the resistance stress seen by the annhiliating dislocations is that of the matrix between the particles, and this would be significantly less than the macroscopically measured yield stress. The key factor determining the resistance stress seen by the annhiliating dislocations is the ratio y*/λ.

We can write the local resistance stress σ_y^* seen by the annhiliating dislocations as:

$$\sigma_y^* = \sigma_{ss} + P * \sigma_{ppt} \tag{11}$$

where σ_{SS} is the solid solution strengthening contribution to the matrix between two annhiliating dislocations, P is the probability for two annhiliating dislocations to meet clusters/precipitates during their annihilation and σ_{ppt} is the cluster or precipitate strengthening contribution to the yield strength.

We can describe this probability, P, by a Poisson distribution involving the ratio $\frac{y^*}{\lambda}$:

$$P = 1 - \exp\left(-\frac{y^*}{\lambda}\right) \tag{12}$$

When λ is small compared to y^*, $P = 1$ (Fig. 9a), when λ is much larger than y^*, $P = 0$ (Fig. 9b).

y^* depends on microstructure and it must be found as the solution to an implicit equation (Eq. (13)):

$$\sigma_{ss} + \left[1 - \exp\left(-\frac{y^*}{\lambda}\right)\right] \cdot \sigma_{ppt} = \frac{Gb}{k_\beta \cdot y^*} \tag{13}$$

The term on the left of Eq. (13) represents the resistance stress seen by the dislocations undergoing a dynamic recovery event, and the term on the right is the interaction stress between the dislocations which drives dynamic recovery.

Solid solutions naturally reduce to the case with probability $P = 0$ and the rate of dynamic recovery reduces to Eq. (14). The grain boundary contribution to the yield strength σ_0 is not considered to affect the dislocation annihilation due to its much larger length scale than y^*.

$$\frac{1}{\beta} = k_\beta \frac{\sigma_{ss}}{G} = k_\beta \frac{\sigma_y - \sigma_0}{G} \tag{14}$$

Using the quantification of the interparticle spacings for the NA and artificially aged AA7050 presented in Figs. 4d and 8c, y^* has been found from Eq. (13) and is plotted for each state, along with λ, in Fig. 10a. Using the values of y^* and λ summarised in Fig. 10a, P is calculated using Eq. (12), the resistance stress seen by the annhiliating dislocations, σ_y^*, is calculated using Eq. (11) and $1/\beta$ is then calculated using Eq. (10). This calculated dynamic recovery rate for the NA and artificially aged AA7050, taking into consideration the effect of the clusters and shearable precipitates, is plotted as red and green points in Fig. 10b. For the most part, the agreement with experimental observations is excellent. It is clear that one may estimate the dynamic recovery rate of these alloys containing shearable clusters or precipitates, if one knows their spacing compared to the critical annhiliation distance.

The calculated dynamic recovery rate for the NA 1670 h sample, using the cluster composition estimated from the APT (green data point) lies a little higher than the experimental measurements (Fig. 10b). This is because the calculated spacing of clusters is smaller when using the APT chemistry (~1.5 nm) compared to the chemistry corresponding to the η' phase (~3 nm) (comparing the red and green filled circle points for NA 1670 h in Fig. 10a). This highlights that it is quite important to quantify accurately the volume fraction of clusters (which strongly influences the cluster spacing) in the NA state, and this depends on the cluster chemistry, which is difficult to measure with confidence when particles are of the order of 1 nm in size [89,91].

The agreement between experimental measurements of dynamic recovery rates and those calculated by considering the balance between the interaction stress between dislocations and the resistance stress seen by the dislocations (which depends on particle spacing) (Fig. 10b), suggests that in these Al alloys, the resistance stress is indeed the dominant factor controlling the dynamic recovery rate at these strain-rates and at room temperature. The different alloys, and different microstructural states in Fig. 10b, all have different amounts of solute in solution. Any effect of this solute in solution on the stacking fault energy, and its subsequent influence on the dynamic recovery event appears to be a 2nd order effect in these alloys, under these conditions.

With the obtained physical understanding of the shape of the dynamic recovery curve as a function of yield strength shown in Fig. 10b, two questions should be asked – how general is this behaviour? And how can it be manipulated to obtain better tensile responses (e.g. better combinations of yield strength and uniform elongation). The latter question is reasonably straightforward. By retarding dynamic recovery, for everything else held equal, the strain hardening rate is increased and this generally improves the elongation (e.g. Fig. 1a) and formability. As the yield strength is increased, the objective would be to remain in the top right hand corner of Fig. 10b, instead of dynamic recovery becoming easier (1/β decreasing) as it does with the artificially aged AA7050. The key to this is to maintain an extremely small particle spacing, smaller than, or close to, the critical annihilation distance y^*. This requires a very high number density of extremely small clusters/precipitates. Already, after artificially ageing at 150 °C, the particle spacing is too large and the annihilating dislocations see mostly the resistance stress of the matrix between the particles.

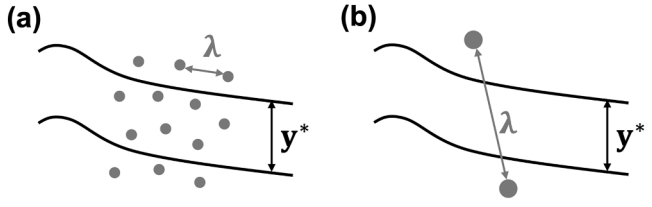

Fig. 9. Schematic representations of the different relative length scales of the inter-particle spacing λ compared to the critical dislocation annihilation distance y^*: (a) $\lambda \ll y^*$ and (b) $\lambda \gg y^*$.

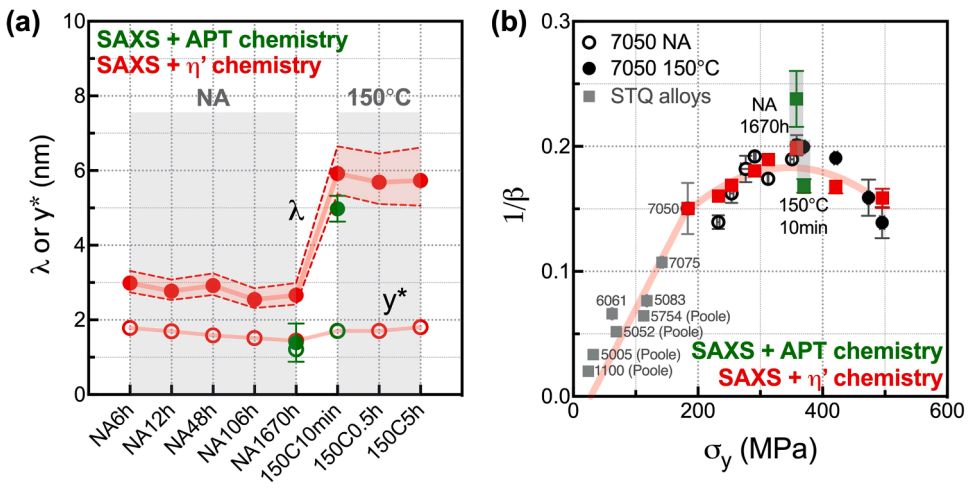

Fig. 10. Summary of the modelling results. (a) The inter-particle spacing λ (full circles) and the critical distance for dislocation annihilation y* (open circles) for the AA7050 NA and 150 °C-aged states. (b) Evolution of the model and experimental $\frac{1}{\beta}$ as a function of σ_y for the AA7050 NA and 150 °C-aged states and other series of Al alloys in the STQ states. The red points are the results based on the particle chemistry assumed to be the equilibrium η' phase calculated by Thermo-Calc. The green points are the results based on the particle chemistry estimated by APT (For interpretation of the references to colour in this figure legend, the reader is referred to the web version of this article.).

4.2. Dynamic recovery behaviour of other 7xxx alloys

To test the generality of the behaviour shown in Fig. 10b, three additional commercial 7xxx alloys have been considered (AA7020, AA7040 and AA7075), both in NA states, and artificially aged states at 120 °C and/or 150 °C. These alloys contain different amounts of solute and hence the precipitation behaviour (volume fraction, size and spacing) is different. Tensile tests were performed in the same way as those shown in Fig. 1, the KM plots were made, and the dynamic recovery behaviour has been quantified by the slope of the stage III hardening curve, β. This data is summarised as 1/β versus experimentally measured yield strength in Fig. 11, and the experimental data for AA7050 is added for comparison. The straight grey line is identical to the straight pink line in Fig. 10b that describes well all of the STQ states shown in Fig. 10b. It also describes quite well the STQ states of the AA7020, AA7040 and AA7075 alloys.

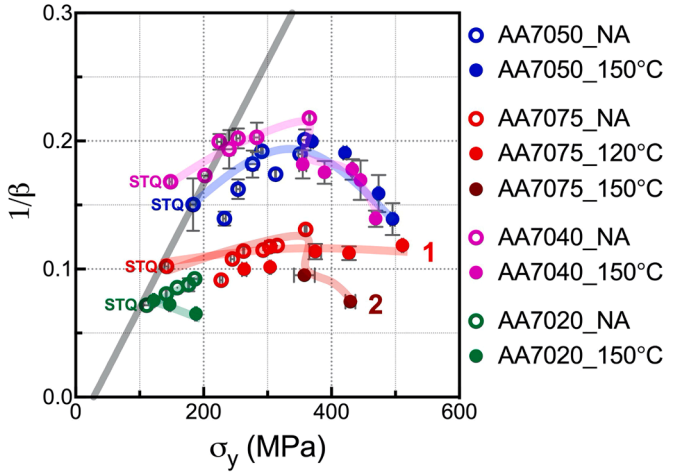

Fig. 11. Evolution of the experimental $\frac{1}{\beta}$ as a function of σ_y for the AA7050 (blue), AA7075 (red and brown), AA7040 (pink) and AA7020 (green) alloys in their STQ, NA (hollow circle) and artificially aged states (full circle). Data from the STQ conditions are labelled. The grey line represents the model $\frac{1}{\beta} = k_\beta \frac{\sigma_y - \sigma_0}{G}$ for solid solutions. The red curve labelled 1 represents the trend for the AA7075 NA and 120 °C aged states. The brown curve labelled 2 represents the trend for the AA7075 NA and 150 °C aged states (For interpretation of the references to colour in this figure legend, the reader is referred to the web version of this article.) .

These alloys all have slightly different solute contents, and this affects the driving force for precipitation and the volume fractions of precipitates formed during NA and artificial ageing, and hence the interparticle spacings – which we have seen in Fig. 10b is the key to understanding the non-monotonic behaviour of the 1/β curves with increasing yield strength. As a rough indication of the relative propensity for precipitation amongst the alloys, one can compare the local equilibrium volume fractions of η' phase at 150 °C. Using Thermo-Calc TCAL4, AA7040 will form 6.7% η' phase. AA7050 6.4%, AA7075 6.0% and AA7020 4.7%. One would expect, under the same solution treatment and ageing conditions, for the number density of particles to be highest in AA7040 and decrease in the order of the volume fractions, and hence the spacing of particles is expected to be smallest for AA7040, followed by AA7050, AA7075, AA7020.

Indeed, the expectations of such comparative precipitation behaviour are reflected well in the dynamic recovery plot in Fig. 11. After NA, dynamic recovery is even more difficult (1/β is highest) in AA7040 compared to AA7050, due to the expected finer cluster spacing. During artificial ageing, when the particle spacing in both alloys is much greater (cf. Fig. 10b), the dynamic recovery behaviour is similar because the solid solution strengthening contributions to the matrix will also be similar.

AA7075 is expected to form fewer particles during NA and artificial ageing and this is the reason for the easier dynamic recovery in Fig. 11 (reduced 1/β) compared to AA7040 and AA7050. Samples of AA7075 were aged at both 120 °C and 150 °C. As can be seen for both types of samples with yield strengths around 400 MPa, the 120°C aged samples show less dynamic recovery (1/β is higher) than the samples aged at 150 °C. This is because the samples aged at the lower temperature will have finer particles (with smaller interparticle spacings) than those aged at the higher temperature of 150 °C.

Finally, the AA7020 alloy contains significantly less solute than the other three alloys. The number density of particles formed in this alloy would be expected to be the smallest of the four alloys and hence the particle spacing will be the largest. As expected, the dynamic recovery behaviour is easiest in this alloy.

The phenomenological model for dynamic recovery presented here, and its modification to take into account the effect of shearable clusters and precipitates, is completely general. We have applied it to the

problem of 7xxx alloys (with a few other STQ other alloys) but it can equally be applied to other Al alloys containing shearable clusters/precipitates such as 2xxx and 6xxx alloys, and likely other alloy systems where the first order effect controlling the dynamic recovery behaviour is the resistance stress seen by the dislocations (as opposed to a SFE effect). In such cases, Fig. 10b demonstrates that it is possible to predict the dynamic recovery behaviour, if the state of precipitation is known.

5. Conclusions

The room temperature dynamic recovery of a range of Al alloys in either the STQ state, or containing shearable clusters/precipitates has been studied in detail using tensile tests. When plotted in the form of a Kocks–Mecking plot, the stage III strain hardening behaviour is well approximated as linear in the alloys considered and the dynamic recovery behaviour has been characterised by the slope, β, of the stage III curve.

The main conclusions of this work are:

1. For a wide range of Al alloys (1xxx, 5xxx, 6xxx and 7xxx) in the STQ state, the dynamic recovery behaviour, expressed as $1/\beta$, is proportional to the experimentally measured yield strength. This suggests that the first order effect controlling dynamic recovery in these alloys is the resistance stress that the matrix exerts on dynamically recovering dislocations, rather than any solute effect on stacking fault energy.
2. When shearable particles are formed in 7xxx alloys, either by natural ageing or artificial ageing, the linear dependence of $1/\beta$ on yield strength is broken. If the clusters/particles are extremely fine, such as those formed during natural ageing, then $1/\beta$ may still increase with increasing yield strength, but at a decreasing rate. As the spacing of the clusters/particles increases, such as during artificial ageing, $1/\beta$ passes through a maximum and then decreases (i.e. dynamic recovery becomes easier) with further increases in yield strength.
3. A simple microstructure-based model is presented to capture the non-monotonic behaviour of $1/\beta$ with increasing yield strength. It is shown that the critical feature controlling the behaviour when shearable particles are added to the microstructure is the ratio of the particle spacing, λ, and the critical annihilation distance, y^*, for dynamic recovery. The model is general and predictive, and can be used as a design tool to help identify microstructures that may show good combinations of strength and strain hardening behaviour.

Declaration of competing interest

The authors declare that they have no known competing financial interests or personal relationships that could have appeared to influence the work reported in this paper.

Acknowledgements

This work was supported by the Australian Research Council through the Discovery Projects Scheme (DP210102714 – CRH & BG). YW gratefully acknowledges the award of the Australian government Research Training Program (RTP). The authors would also like to express thanks for the use of equipment within the Monash X-Ray Platform (MXP). XC acknowledges the financial support from the China Scholarship Council (number: 201806310105). We thank U. Tezins, A. Sturm, and C. Broß for technical support at the FIB/APT facilities at MPIE. The authors are especially grateful to Dr Christophe Sigli from Constellium for donating the AA7020 and AA7040 alloys used in this work.

Supplementary materials

Supplementary material associated with this article can be found, in the online version, at doi:10.1016/j.actamat.2023.119643.

References

[1] E.A. Starke, J.T. Staley, Application of modern aluminum alloys to aircraft, Prog. Aerosp. Sci. 32 (2–3) (1996) 131–172.
[2] W.S. Miller, L. Zhuang, J. Bottema, A.J. Wittebrood, P. De Smet, A. Haszler, et al., Recent development in aluminium alloys for the automotive industry, Mater. Sci. Eng.: A 280 (1) (2000) 37–49.
[3] I. Polmear, D. St John, J.F. Nie, M Qian, Light Alloys: Metallurgy of the Light Metals, Elsevier Science & Technology, Oxford, UK, 2017, pp. 1–525.
[4] M.O. Speidel, Stress corrosion cracking of aluminum alloys, Metallur. Transact. A. 6 (4) (1975) 631–651.
[5] J.R. Davis, Corrosion of Aluminum and Aluminum Alloys, ASM International, Materials Park, United State, 1999.
[6] H. Ezuber, A. El-Houd, F. El-Shawesh, A study on the corrosion behavior of aluminum alloys in seawater, Mater. Des. 29 (4) (2008) 801–805.
[7] N. Birbilis, B. Hinton, Corrosion and corrosion protection of aluminium, editor, in: R Lumley (Ed.), Fundamentals of Aluminium Metallurgy: Production, Processing and Applications, Woodhead Publishing Limited, Cambridge, UK, 2010, pp. 574–604.
[8] G.G. Garrett, J.F. Knott, The influence of compositional and microstructural variations on the mechanism of static fracture in aluminum alloys, Metall. Trans. A 9 (9) (1978) 1187–1201.
[9] G.M. Ludtka, D.E. Laughlin, The influence of microstructure and strength on the fracture mode and toughness of 7xxx series aluminum alloys, Metall. Trans. A 13 (3) (1982) 411–425.
[10] E.J. Lavernia, T.S. Srivatsan, F.A. Mohamed, Strength, deformation, fracture behaviour and ductility of aluminium-lithium alloys, J. Mater. Sci. 25 (2) (1990) 1137–1158.
[11] M. Nakai, T. Eto, New aspect of development of high strength aluminum alloys for aerospace applications, Mater. Sci. Eng. A 285 (1–2) (2000) 62–68.
[12] D. Lassance, D. Fabrègue, F. Delannay, T. Pardoen, Micromechanics of room and high temperature fracture in 6xxx Al alloys, Prog. Mater Sci. 52 (1) (2007) 62–129.
[13] T.F. Morgeneyer, M.J. Starink, I. Sinclair, Evolution of voids during ductile crack propagation in an aluminium alloy sheet toughness test studied by synchrotron radiation computed tomography, Acta Mater. 56 (8) (2008) 1671–1679.
[14] J.F. Knott, Fracture resistance in aluminium. Fundamentals of Aluminium Metallurgy: Production, Processing and Applications, Woodhead Publishing Limited, 2010, pp. 538–573.
[15] K.T.V. Rao, R.O. Ritchie, Fatigue of aluminium-lithium alloys, Int. Mater. Rev. 37 (1) (1992) 153–186.
[16] A. Heinz, A. Haszler, C. Keidel, S. Moldenhauer, R. Benedictus, W.S. Miller, Recent development in aluminium alloys for aerospace applications, Mater. Sci. Eng. A 280 (1) (2000) 102–107.
[17] D.A. Lados, Design for fatigue crack growth resistance in aluminum alloys. Fundamentals of Aluminium Metallurgy: Production, Processing and Applications, Woodhead Publishing Limited, 2010, pp. 504–537, p.
[18] H. Hayashi, T. Nakagawa, Recent trends in sheet metals and their formability in manufacturing automotive panels, J. Mater. Process. Tech. 46 (3–4) (1994) 455–487.
[19] G.B. Burger, A.K. Gupta, P.W. Jeffrey, D.J. Lloyd, Microstructural control of aluminum sheet used in automotive applications, Mater. Charact. 35 (1) (1995) 23–39.
[20] J. Hirsch, Aluminium sheet fabrication and processing. Fundamentals of Aluminium Metallurgy: Production, Processing and Applications, Woodhead Publishing Limited, 2010, pp. 719–746.
[21] D. Raabe, D. Ponge, P.J. Uggowitzer, M. Roscher, M. Paolantonio, C. Liu, et al., Making sustainable aluminum by recycling scrap: the science of “dirty” alloys, Prog. Mater Sci. 128 (February) (2022).
[22] O. Engler, Effect of precipitation state on plastic anisotropy in sheets of the age-hardenable aluminium alloys AA 6016 and AA 7021, Mater. Sci. Eng.: A 830 (August 2021) (2022), 142324.
[23] T. Moons, P. Ratchev, P. De Smet, B. Verlinden, P. Van Houtte, A comparative study of two Al-Mg-Si alloys for automotive applications, Scr. Mater. 35 (8) (1996) 939–945.
[24] A. Perovic, D.D. Perovic, G.C. Weatherly, D.J. Lloyd, Precipitation in aluminum alloys AA6111 and AA6016, Scripta Materialia. 41 (7) (1999) 703–708.
[25] Y. Birol, Pre-aging to improve bake hardening in a twin-roll cast Al-Mg-Si alloy, Mater. Sci. Eng.: A 391 (1–2) (2005) 175–180.
[26] R. Raj, Development of a processing map for use in warm-forming and hot-forming processes, Metallur. Transacti. A, Phys. Metallur. Mater. Sci. 12 A (6) (1981) 1089–1097.
[27] A. Deschamps, G. Fribourg, Y. Bréchet, J.L. Chemin, C.R. Hutchinson, In situ evaluation of dynamic precipitation during plastic straining of an Al-Zn-Mg-Cu alloy, Acta Mater. 60 (5) (2012) 1905–1916.
[28] M. Kumar, N.G. Ross, Influence of temper on the performance of a high-strength Al-Zn-Mg alloy sheet in the warm forming processing chain, J. Mater. Process. Technol. 231 (2016) 189–198.
[29] L. Couturier, A. Deschamps, F. De Geuser, F. Fazeli, W.J. Poole, An investigation of the strain dependence of dynamic precipitation in an Al-Zn-Mg-Cu alloy, Scr. Mater. 136 (2017) 120–123.
[30] J.A. Österreicher, M.A. Tunes, F. Grabner, A. Arnoldt, T. Kremmer, S. Pogatscher, et al., Warm-forming of pre-aged Al-Zn-Mg-Cu alloy sheet, Mater. Des. 193 (2020), 108837.
[31] M. Bignon, P. Shanthraj, J.D. Robson, Modelling dynamic precipitation in pre-aged aluminium alloys under warm forming conditions, Acta Mater. 234 (2022), 118036.

[32] S. DiCecco, M. Di Ciano, N. Baghbanaghaie, S. Esmaeili, M.A. Wells, M. J. Worswick, Warm aging of pre-aged AA6013 sheet and its relevance to room temperature and warm forming applications—experimental and modeling analyses, J. Mater. Eng. Perform. (i) (2023).
[33] L.M. Cheng, W.J. Poole, J.D. Embury, D.J. Lloyd, The influence of precipitation on the work-hardening behavior of the aluminum alloys AA6111 and AA7030, Metallur. Mater. Transact. A. 34 A (11) (2003) 2473–2481.
[34] W.J. Poole, X. Wang, D.J. Lloyd, J.D. Embury, The shearable-non-shearable transition in Al-Mg-Si-Cu precipitation hardening alloys: implications on the distribution of slip, work hardening and fracture, Philos. Mag. 85 (2005) 3113–3135, 26-27 SPEC. ISS.
[35] C. Gallais, A. Simar, D. Fabregue, A. Denquin, G. Lapasset, B. de Meester, et al., Multiscale analysis of the strength and ductility of AA 6056 aluminum friction stir welds, Metall. Mater. Trans. A 38 (5) (2007) 964–981.
[36] K.O. Pedersen, O.G. Lademo, T. Berstad, T. Furu, O.S. Hopperstad, Influence of texture and grain structure on strain localisation and formability for AlMgSi alloys, J. Mater. Process. Technol. 200 (1–3) (2008) 77–93.
[37] M.R. Stoudt, L.E. Levine, A. Creuziger, J.B. Hubbard, The fundamental relationships between grain orientation, deformation-induced surface roughness and strain localization in an aluminum alloy, Mater. Sci. Eng.: A 530 (1) (2011) 107–116.
[38] A. Davidkov, M.K. Jain, R.H. Petrov, D.S. Wilkinson, R.K. Mishra, Strain localization and damage development during bending of Al-Mg alloy sheets, Mater. Sci. Eng.: A 550 (2012) 395–407.
[39] T.F. Morgeneyer, T. Taillandier-Thomas, L. Helfen, T. Baumbach, I. Sinclair, S. Roux, et al., In situ 3-D observation of early strain localization during failure of thin Al alloy (2198) sheet, Acta Mater. 69 (2014) 78–91.
[40] V.K. Barnwal, R. Raghavan, A. Tewari, K. Narasimhan, S.K. Mishra, Effect of microstructure and texture on forming behaviour of AA-6061 aluminium alloy sheet, Mater. Sci. Eng.: A 679 (June 2016) (2017) 56–65.
[41] V Gerold, Precipitation hardening, editor, in: FRN Nabarro (Ed.), Dislocations in Solids, North-Holland Pub. Co., New York, US, 1979.
[42] A.J Ardell, Precipitation hardening, Metall. Trans. A 16 (1985) 2131–2165.
[43] H.R. Shercliff, M.F. Ashby, A process model for age hardening of aluminium alloys-I. The model, Acta Metall. Mater. 38 (10) (1990) 1789–1802.
[44] H.R. Shercliff, M.F. Ashby, A process model for age hardening of aluminium alloys-II. Applications of the model, Acta Metall. Mater. 38 (10) (1990) 1803–1812.
[45] A. Deschamps, Y. Brechet, Influence of predeformation and ageing of an Al-Zn-Mg Alloy-II. Modeling of precipitation kinetics and yield stress, Acta Mater. 47 (1) (1998) 293–305.
[46] S. Esmaeili, D.J. Lloyd, W.J. Poole, A yield strength model for the Al-Mg-Si-Cu alloy AA6111, Acta Mater. 51 (8) (2003) 2243–2257.
[47] S. Esmaeili, D.J. Lloyd, W.J. Poole, Modeling of precipitation hardening for the naturally aged Al-Mg-Si-Cu alloy AA6111, Acta Mater. 51 (12) (2003) 3467–3481.
[48] S. Esmaeili, D.J. Lloyd, Modeling of precipitation hardening in pre-aged AlMgSi (Cu) alloys, Acta Mater. 53 (20) (2005) 5257–5271.
[49] J. da Costa Teixeira, D.G. Cram, L. Bourgeois, T.J. Bastow, A.J. Hill, C. R. Hutchinson, On the strengthening response of aluminum alloys containing shear-resistant plate-shaped precipitates, Acta Mater. 56 (20) (2008) 6109–6122.
[50] J.F. Nie, B.C Muddle, Strengthening of an Al-Cu-Sn alloy by deformation-resistant precipitate plates, Acta Mater. 56 (14) (2008) 3490–3501.
[51] B. Holmedal, Strength contributions from precipitates, Philos. Mag. Lett. 95 (12) (2015) 594–601.
[52] Z. Ma, J.D. Robson, Understanding the effect of deformation combined with heat treatment on age hardening of Al–Zn–Mg–Cu alloy AA7075, Mater. Sci. Eng.: A 878 (June) (2023).
[53] J.F. Nie, B.C. Muddle, I.J. Polmear, The effect of precipitate shape and orientation on dispersion strengthening in high strength aluminium alloys, Mater. Sci. Forum 217–222 (PART 2) (1996) 1257–1262.
[54] D. Bardel, M. Perez, D. Nelias, A. Deschamps, C.R. Hutchinson, D. Maisonnette, et al., Coupled precipitation and yield strength modelling for non-isothermal treatments of a 6061 aluminium alloy, Acta Mater. 62 (1) (2014) 129–140.
[55] B. Holmedal, E. Osmundsen, Q. Du, Precipitation of non-spherical particles in aluminum alloys part I: generalization of the Kampmann–Wagner numerical model, Metall. Mater. Trans. A 47 (1) (2016) 581–588.
[56] Q. Du, B. Holmedal, J. Friis, C.D. Marioara, Precipitation of non-spherical particles in aluminum alloys part II: numerical simulation and experimental characterization during aging treatment of an Al-Mg-Si alloy, Metall. Mater. Trans. A 47 (1) (2016) 589–599.
[57] Y. Li, B. Holmedal, H. Li, L. Zhuang, J. Zhang, Q. Du, Precipitation and strengthening modeling for disk-shaped particles in aluminum alloys: size distribution considered, Materialia. 4 (October) (2018) 431–443.
[58] P. Haasen, Solution hardening in F. C. C. metals, Dislocation. Solid. 4 (1980) 155–189.
[59] Ø. Ryen, O. Nijs, E. Sjölander, B. Holmedal, H.E. Ekström, E. Nes, Strengthening mechanisms in solid solution aluminum alloys, Metall. Mater. Trans. A 37 (6) (2006) 1999–2006.
[60] E.L. Huskins, B. Cao, K.T. Ramesh, Strengthening mechanisms in an Al-Mg alloy, Mater. Sci. Eng.: A 527 (6) (2010) 1292–1298.
[61] G.P.M. Leyson, L.G. Hector, W.A. Curtin, Solute strengthening from first principles and application to aluminum alloys, Acta Mater. 60 (9) (2012) 3873–3884.
[62] Z. Liu, V. Mohles, Solution strengthening of various elements in aluminium alloys, Mater. Sci. Forum 794–796 (2014) 473–478.
[63] C. Varvenne, G.P.M. Leyson, M. Ghazisaeidi, W.A. Curtin, Solute strengthening in random alloys, Acta Mater. 124 (2017) 660–683.
[64] B. Holmedal, E. Nes, K. Marthinsen, work hardening of aluminium alloys, editor, in: J Hirsh (Ed.), Virtual Fabrication of Aluminium products : Microstructural Modeling in Industrial Aluminum Production, WILEY-VCH Verlag GmbH & Co. KGaA, 2005, pp. 129–155.
[65] W.J. Poole, J.D. Embury, D.J. Lloyd, Work hardening in aluminium alloys, editor, in: R Lumley (Ed.), Fundamentals of Aluminium Metallurgy: Production, Processing and Applications, Woodhead Publishing Limited, Cambridge, UK, 2010, pp. 307–344.
[66] K. Marthinsen, S. Abtahi, B. Holmedal, J. Friis, E. Nes, T. Furu, Modelling the work hardening behaviour of AlMgMn alloys, Mater. Sci. Forum 638–642 (1) (2010) 285–290.
[67] G. Fribourg, Y. Bréchet, A. Deschamps, A. Simar, Microstructure-based modelling of isotropic and kinematic strain hardening in a precipitation-hardened aluminium alloy, Acta Mater. 59 (9) (2011) 3621–3635.
[68] Q. Zhao, B. Holmedal, Modelling work hardening of aluminium alloys containing dispersoids, Philos. Mag. 93 (23) (2013) 3142–3153.
[69] A. Abel, R.K. Ham, The cyclic strain behaviour of crystals of aluminum-4 wt.% copper-i. the bauschinger effect, Acta Metall. 14 (11) (1966) 1489–1494.
[70] L.M. Brown, W.M. Stobbs, The work-hardening of copper-silica i. A model based on internal stresses, with no plastic relaxation, Philos. Mag. 23 (185) (1971) 1201–1233.
[71] R.E. Stoltz, R.M. Pelloux, The Bauschinger effect in precipitation strengthened aluminum alloys, Metall. Trans. A 7 (8) (1976) 1295–1306.
[72] G.D. Moan, J.D. Embury, A study of the bauschinger effect in AlCu alloys, Acta Metall. 27 (5) (1979) 903–914.
[73] S.F. Corbin, D.S. Wilkinson, J.D. Embury, The Bauschinger effect in a particulate reinforced Al alloy, Mater. Sci. Eng.: A 207 (1) (1996) 1–11.
[74] H. Proudhon, W.J. Poole, X. Wang, Y. Bréchet, The role of internal stresses on the plastic deformation of the Al-Mg-Si-Cu alloy AA6111, Philosoph. Magaz. 88 (5) (2008) 621–640.
[75] J. da Costa Teixeira, L. Bourgeois, C.W. Sinclair, C.R. Hutchinson, The effect of shear-resistant, plate-shaped precipitates on the work hardening of Al alloys: towards a prediction of the strength-elongation correlation, Acta Mater. 57 (20) (2009) 6075–6089.
[76] I. Westermann, O.S. Hopperstad, K. Marthinsen, B. Holmedal, Ageing and work-hardening behaviour of a commercial AA7108 aluminium alloy, Mater. Sci. Eng.: A 524 (1–2) (2009) 151–157.
[77] Y. Estrin, Dislocation-density-related constitutive modeling, editors, in: AS Krausz, K Krausz (Eds.), Unified Constitutive Laws of Plastic Deformation, Elsevier Science & Technology, London UK, 1996, pp. 69–106.
[78] A. Simar, Y. Bréchet, B. de Meester, A. Denquin, T. Pardoen, Sequential modeling of local precipitation, strength and strain hardening in friction stir welds of an aluminum alloy 6005A-T6, Acta Mater. 55 (18) (2007) 6133–6143.
[79] H. Mecking, U.F. Kocks, Kinetics of flow and strain-hardening, Acta Metall. 29 (11) (1981) 1865–1875.
[80] Y. Estrin, H. Mecking, A unified phenomenological description of work hardening and creep based on one-parameter models, Acta Metall. 32 (1) (1984) 57–70.
[81] A. Deschamps, Y. Bréchet, C.J. Necker, S. Saimoto, J.D. Embury, Study of large strain deformation of dilute solid solutions of Al-Cu using channel-die compression, Mater. Sci. Eng. A 207 (2) (1996) 143–152.
[82] J. Hirsch, Aluminium in innovative light-weight car design, Mater. Trans. 52 (5) (2011) 818–824.
[83] W.Z. Han, A. Vinogradov, C.R. Hutchinson, On the reversibility of dislocation slip during cyclic deformation of Al alloys containing shear-resistant particles, Acta Mater. 59 (9) (2011) 3720–3736.
[84] F. De Geuser, A. Deschamps, Precipitate characterisation in metallic systems by small-angle X-ray or neutron scattering, C.R. Phys. 13 (3) (2012) 246–256.
[85] A. Deschamps, F. De Geuser, Quantitative characterization of precipitate microstructures in metallic alloys using small-angle scattering, Metall. Mater. Trans. A 44 (1) (2013) 77–86.
[86] A. Deschamps, F. Bley, F. Livet, D. Fabregue, L David, In-situ small-angle X-ray scattering study of dynamic precipitation in an Al-Zn-Mg-Cu alloy, Philos. Mag. 83 (6) (2003) 677–692.
[87] De Geuser F, W Lefebvre, Determination of matrix composition based on solute-solute nearest-neighbor distances in atom probe tomography, Microsc. Res. Tech. 74 (3) (2011) 257–263.
[88] H. Zhao, B. Gault, D. Ponge, D. Raabe, F. De Geuser, Parameter free quantitative analysis of atom probe data by correlation functions: application to the precipitation in Al-Zn-Mg-Cu, Scr. Mater. 154 (2018) 106–110.
[89] F. De Geuser, B. Gault, Metrology of small particles and solute clusters by atom probe tomography, Acta Mater. 188 (2020) 406–415.
[90] A. Guinier, G. Fournet, C.B. Walker, K.L. Yudowitch, Small-angle Scattering of X-rays, Wiley, New York, US, 1955.
[91] B. Gault, A. Chiaramonti, O. Cojocaru-Mirédin, P. Stender, R. Dubosq, C. Freysoldt, et al., Atom probe tomography, Nat. Rev. Method. Primer. 1 (1) (2021).
[92] P. Zhang, K. Shi, J. Bian, J. Zhang, Y. Peng, G. Liu, et al., Solute cluster evolution during deformation and high strain hardening capability in naturally aged Al–Zn–Mg alloy, Acta Mater. 207 (2021), 116682.
[93] A. Deschamps, T.J. Bastow, F. De Geuser, A.J. Hill, C.R. Hutchinson, In situ evaluation of the microstructure evolution during rapid hardening of an Al-2.5Cu-1.5Mg (wt.%) alloy, Acta Mater. 59 (8) (2011) 2918–2927.

[94] G. Sha, A. Cerezo, Early-stage precipitation in Al-Zn-Mg-Cu alloy (7050), Acta Mater. 52 (15) (2004) 4503–4516.
[95] S. Shah, E. Thronsen, C. Hatzoglou, S. Wenner, C.D. Marioara, R. Holmestad, et al., Effect of cyclic ageing on the early-stage clustering in Al–Zn–Mg(-Cu) alloys, Mater. Sci. Eng.: A 846 (May) (2022).
[96] A. Lervik, E. Thronsen, J. Friis, C.D. Marioara, S. Wenner, A. Bendo, et al., Atomic structure of solute clusters in Al–Zn–Mg alloys, Acta Mater. 205 (2021), 116574.